Author's Accepted Manuscript

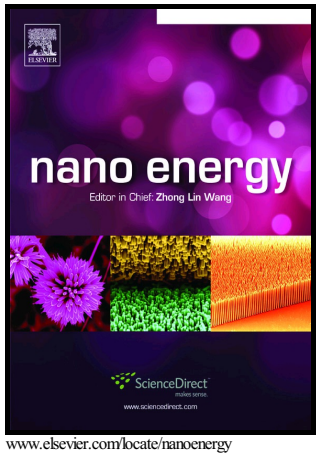

www.elsevier.com/locate/nanoenergy

Recessed Deposition of TiN into N-doped Carbon as a Cathode Host for Superior Li-S Batteries Performance

Zhenyu Xing, Gaoran Li, Serubbabel Sy, Zhongwei Chen

PII: S2211-2855(18)30678-5
DOI: https://doi.org/10.1016/j.nanoen.2018.09.034
Reference: NANOEN3039

To appear in: *Nano Energy*

Received date: 9 July 2018
Revised date: 14 September 2018
Accepted date: 16 September 2018

Cite this article as: Zhenyu Xing, Gaoran Li, Serubbabel Sy and Zhongwei Chen, Recessed Deposition of TiN into N-doped Carbon as a Cathode Host for Superior Li-S Batteries Performance, *Nano Energy,* https://doi.org/10.1016/j.nanoen.2018.09.034

Recessed Deposition of TiN into N-doped Carbon as a Cathode Host for Superior Li-S Batteries Performance

Zhenyu Xing[a, b1], Gaoran Li[b,1], Serubbabel Sy[b], and Zhongwei Chen[b]*

[a]School of Chemistry and Environment, South China Normal University, Guangzhou, 510006, PR China

[b]Department of Chemical Engineering, Waterloo Institute for Nanotechnology, Waterloo Institute for Sustainable Energy, University of Waterloo, 200 University Avenue W, Waterloo, Ontario N2L 3G1, Canada

E-mail: zhwchen@uwaterloo.ca

Abstract

In this work, we put forward a novel cathode host for Li-S batteries by loading titanium nitride (TiN) nanoparticles into the pores of N-doped carbon as a proof-of-concept. The selection of TiN arises from its strong binding ability with polysulfide and its exceptionally high conductivity of 5×10^6 S/m. As for N-doped porous carbon, it provides necessary physical adsorption and extra chemical adsorption sites from the N-doping. Besides the above advantages, the most substantial merit endowed to this structure is the pore-loaded TiN design. The carbon pore size confines the TiN precursors to the nanoscale and prevents otherwise subsequent agglomeration of TiN nanoparticles. Moreover, the pore-loaded TiN design, with fully exposed adsorptive surface and highly dispersed adsorptive sites, guards against the blocking of future sulfur infiltration and Li^+ diffusion. The advantages of the TiN

[1] These authors equally contributed to the paper.

loaded N-doped carbon are finally confirmed by electrochemical evaluations. The capacity is found up to be 1338 mAh/g at a current density of 0.2C and 690 mAh/g at a current density of 5C (where 1C = 1672 mAh/g). For durability evaluations, the capacity is maintained at 700 mAh/g after 800 cycles with a mere decay of 0.04 % per cycle. Lastly, the feasibility of a high mass loading with 7 mg/cm^2 is demonstrated.

Graphical abstract

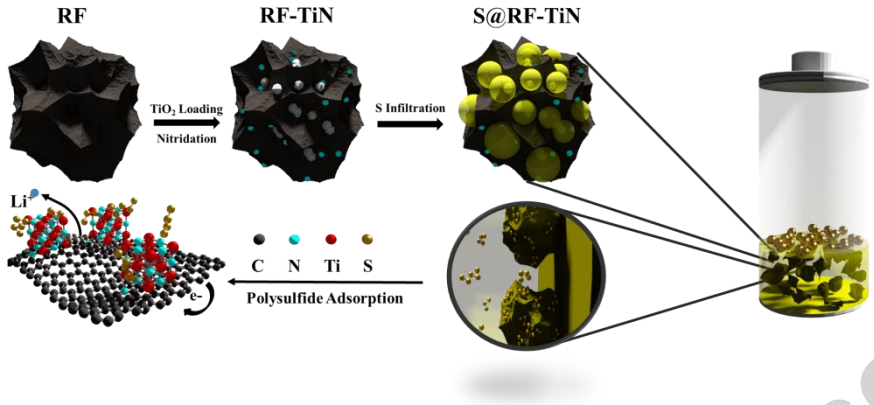

Keywords:

lithium sulfur batteries, polysulfide adsorption, high mass loading, recessed deposition of TiN, N-doped porous carbon

Introduction

Finding an alternative energy source to replace fossil fuels is becoming a necessity for a sustainable society [1, 2]. Nowadays, Li-ion batteries (LIBs) have gained tremendous success in the portable electronics and electric vehicles market [3, 4]. Albeit the fact that LIBs have been commercialized for over 27 years, the energy density of 387 Wh/kg have persistently been unable to meet the ever-increasing requirement of a longer discharge time [5-7]. For this reason, researchers have begun to refocus their attention to Li-S batteries, which possess a significantly higher theoretical energy density, of up to 2600 Wh/kg [8-10]. However, the higher energy density does not guarantee a satisfactory substitute for LIBs unless the drawbacks of Li-S batteries are addressed. Li-S batteries are based on a conversion reaction between a Li-metal anode and a sulfur cathode with polysulfide as the intermediate product [11]. As widely known, the sharp drop in the capacity under a high current density is due to the higher overpotential required to compensate for the insulating S_8 and Li_2S products when charging and discharging, respectively. Moreover, constant dissolution of polysulfide and related shuttle effects lead to a capacity fading and low Coulombic efficiency [12]. Thus, increasing conductivity and decreasing polysulfide dissolution are the two promising strategies to address the aforementioned deficiencies on the cathode side of Li-S batteries [13].

Researchers have found that the low conductivity of S_8/Li_2S can be dramatically improved by depositing sulfur on a conductive substrate, or more preferably, infiltrating sulfur into a porous carbon host [14, 15]. As for polysulfide dissolution, it cannot be solved solely by chemical adsorption based on polar-polar interaction nor only by physical confinement from the porous framework [16, 17]. Rather, combining physical adsorption and chemical adsorption has proven to be highly effective, which may include doping heteroatoms into porous carbon or preparing a porous framework with suitable polarity, considering the different polarity requirement from S_8 or Li_2S precipitation [18-25]. Doping heteroatoms increases the chemical adsorption, however, the interaction between heteroatoms and

polysulfide is very weak. Compared with heteroatoms, metal sulfide, carbide, nitride and other polysulfide suppressants show unquestionably higher binding energies with polysulfide [26-28]. However, the higher molecular weight hinders them when incorporating a sufficient amount of the suppressant into a porous structure to achieve the same amount of physical confinement as porous carbon. Therefore, a rationally designed structure for the sulfur host, which combines physical confinement with chemical adsorption yet maintain a high conductivity, is still lacking.

Herein, we put forward a novel cathode host by loading titanium nitride (TiN) nanoparticles into the pores of N-doped carbon as a proof-of-concept. The rationale behind the selection of TiN arise from its strong binding ability with polysulfide and its exceptionally high theoretical conductivity of 5×10^6 S/m, which is four orders of magnitude higher than that of typical porous carbon [29-33]. As for N-doped porous carbon, it provides the necessary physical adsorption due to the porous structure and extra chemical adsorption sites from the N-doping. In addition to the preceding advantages, the most substantial merit endowed to this structure is the pore-loaded TiN design. The carbon pore size confines the TiN precursors to the nanoscale and prevents otherwise subsequent agglomeration of TiN nanoparticles in the nitridation process. Compared with bulk TiN, the derived TiN nanoparticles have a much stronger polysulfide adsorption capability due to their fully exposed crystal planes, a widely recognized surface effect within nanomaterials.[29, 30, 34, 35] Moreover, the pore-loaded TiN design, with fully exposed adsorptive surface and highly dispersed adsorptive sites, guards against the blocking of future sulfur infiltration and Li^+ diffusion assuming TiN nanoparticles are loaded into the pores rather than merely on the surface. The advantages of the TiN loaded N-doped carbon are finally confirmed by electrochemical evaluations. The capacity was found to be remarkably high, up to 1338 mAh/g at a current density of 0.2C and 690 mAh/g at a current density of 5C (where 1C = 1672 mAh/g). For durability evaluations,

the capacity was maintained at 700 mAh/g after 800 cycles with a mere decay of 0.04% per cycle. Lastly, the feasibility of a high mass loading of 7 mg/cm^2 was demonstrated.

Experimental Section

Materials Synthesis

Preparation of RF: RF carbon is prepared using a typical hard-template method. Specifically, Ludox colloidal silica of 7 nm and 22 nm is mixed at a weight ratio of 1.66 g : 32 g under sonication for 24h. After dried at room temperature for one week, the obtained SiO_2 template is immersed into a Resorcinol/Formaldehyde solution at a mole ratio 1:2 in an ice bath for 3h. Subsequently, the infiltrated SiO_2 is dried under 85 ºC for 24h and 120 ºC for 24h. With another repeated infiltration process, the twice-infiltrated SiO_2 is heated under Argon atmosphere at 900 ºC for 4h with a ramping rate of 10 ºC /min. Finally, RF carbon is obtained after removal of the SiO_2 template via dilute HF washing.

Preparation of RF-TiN: Firstly, As-prepared RF absorbs water vapor at 80 ºC, then is immersed into titanium tetraisopropoxide/1, 3 dioxolane solution with 5 vol% for 1h. After filtration in the glove box, the collected sample is heated NH_3 in the tube furnace at 850 ºC for 5h.

Preparation of TiN-NP: TiN-NP is synthesized by heating commercial 5nm TiO_2 powder under NH_3 in the tube furnace at 850 ºC for 1h.

Characterization Methods

X-ray diffraction (XRD) patterns were recorded using a MiniFlex 600 Rigaku Diffractometer with Cu Kα irradiation (λ= 1.5406 Å). To collect Raman spectra, a 514 nm laser source was employed. The morphology was investigated by SEM (LEO FESEM 1530). Transmission electron microscopy (TEM) images were collected by TEM (JEOL 2010F TEM/STEM). Nitrogen sorption measurements were performed on Autosorb iQ Station 1. XPS

measurements were performed in a Thermo Scientific K-Alpha spectrometer. For the electronic conductivity, sample powder was measured by the direct current polarization test under 2 tons pressure in the stainless steel cell of 10 mm diameter.

Electrochemical Measurements:

RF, RF-TiN, and TiN-NP was impregnated with sulfur of 70 wt% at 155 ºC for 6h. The slurry consist of 80 wt% sulfur@host, 10 wt% carbon black (Super-P) and 10 wt% polyvinylidene fluoride (PVDF) as the binder. Via the doctor-blade method, the slurry was coated on aluminum foil and subsequently dried at 60 °C overnight under vacuum conditions and transferred into the glove box immediately after the drying process. Coin cells (2032) were assembled: with the as-prepared electrode (14 mm in diameter) as the working electrode, lithium metal as the counter/reference electrode, Celegard 2500 membrane as a separator and stainless steel spring (1mm in thickness) and spacer (1mm in thickness) as a spacer, in an argon-filled glove box. The electrolyte was prepared by dissolving 1M LiTFSI with 0.2 M lithium nitrate into a mixture of 1,2-dimethoxyethane (DME) and 1,3-dioxolane (DOL) (1:1 by volume). The active mass loading was around 1.5 mg/cm^2 for the tests of galvanostatic charge-discharge, CV, EIS, rate capability and long cycle life in Figure 4 and Figure 5. The active mass loading was around 1.5, 3, 5, and 7 mg/cm^2 for the tests of high-mass loading in Figure 6. The ratio for electrolyte/sulfur in each cell is about 16 ml/g_{sulfur} for the mass loading of 1.5 mg/cm^2 while 10 ml/g_{sulfur} for the mass loading of 3.1 mg/cm^2, 4.8 mg/cm^2 and 7.0 mg/cm^2. [36]. The electrochemical measurements were performed on LAND battery cycler for galvanostatic charge-discharge test and Gamry 5000E workstation for CV test, where the voltage range was from 0.01 to 2 V versus Li^+/Li. EIS results were obtained by Gamry 5000E workstation with the frequency range of 0.1 Hz–100 kHz.

Result and Discussion

The porous carbon was prepared from the carbonization of resorcinol-formaldehyde resin after removing SiO_2 template, which will be referred to as RF with morphology shown in **Figure S1**. Then, the as-prepared RF with absorbed water vapor was soaked in titanium (IV) isopropoxide organic solution, during which TiO_2 was loaded into the RF pores. After nitridation in the ammonia, the TiO_2-loaded RF is converted into TiN-loaded N-doped RF, which will herein be referred to as RF-TiN, the morphology of which is shown in **Figure S2**. The whole process and RF-TiN nanostructure is depicted in **Schematic 1**. As a reference, pure TiN nanoparticle (TiN-NP) was also synthesized after nitridation of commercial TiO_2 nanoparticle, the morphology of which is shown in **Figure S3**.

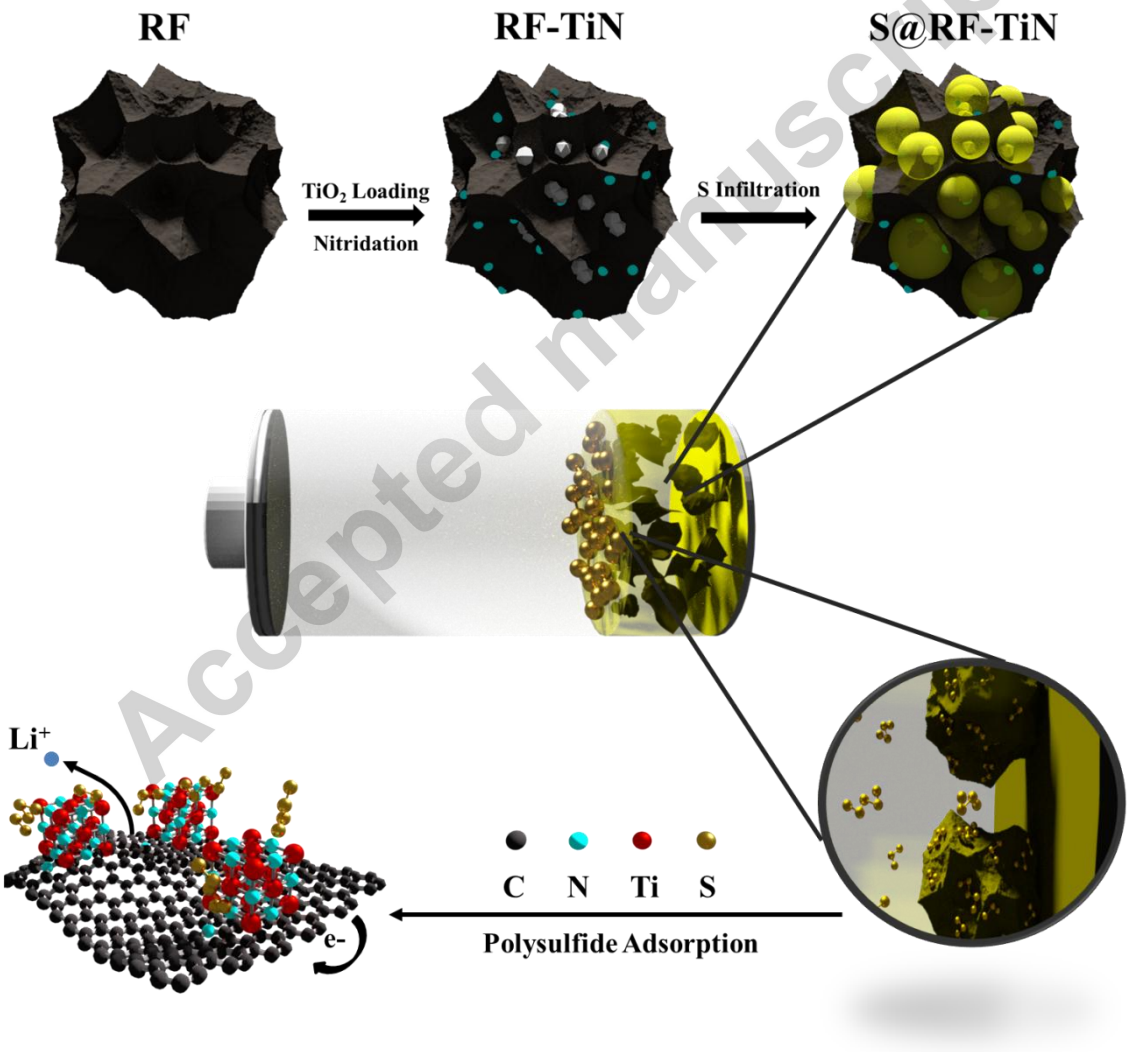

Schematic 1 Schematic of the preparation of RF-TiN and S@RF-TiN and its application in

the Li-S battery. The black host is the RF carbon, while particles are loaded TiN nanoparticles, cyan dots represent the doped N atoms, and yellow spheres correspond to the infiltrated sulfur molecules.

As the X-ray diffraction (XRD) results shown, the newly formed peaks of RF-TiN in **Figure 1a** can be indexed to the TiN cubic structure with a space group Fm-3m (225). Based on the Scherrer equation, the average crystallite size was estimated to be 7.5 nm along the (200) direction and 25.5 nm along the (111) direction, respectively. Moreover, the carbon host was confirmed by the (002) peak around 26º, a typical feature for carbon. It should be noted here that the average crystallite size along (002) direction of the carbon host in RF-TiN compared with RF, increased from 1.24 nm to 1.46 nm. This change was due to the preferential etching of smaller carbon crystallites by NH_3 [37, 38]. With the addition of TiN and the increased crystallite size of carbon host, the conductivity of RF-TiN was measured at 63 S/m, much higher than the 23 S/m of RF.

Aside from XRD, the existence of TiN was also confirmed by the well-matching Raman bands of RF-TiN and TiN NP, located between 160 cm^{-1} to 610 cm^{-1} in **Figure 1b**. As for the carbon host, the D band at 1350 cm^{-1} and G band 1580 cm^{-1} are assigned to the A_{1g} vibration mode of C_6 ring defects and E_{2g} mode of sp^2 carbon, respectively [39-41]. Thus far, the TiN/carbon composite has been completely confirmed by the XRD and Raman results. Based on the thermal gravimetric analysis (TGA) result in **Figure S4**, the amount of loaded TiN was determined to be 27 wt. %.

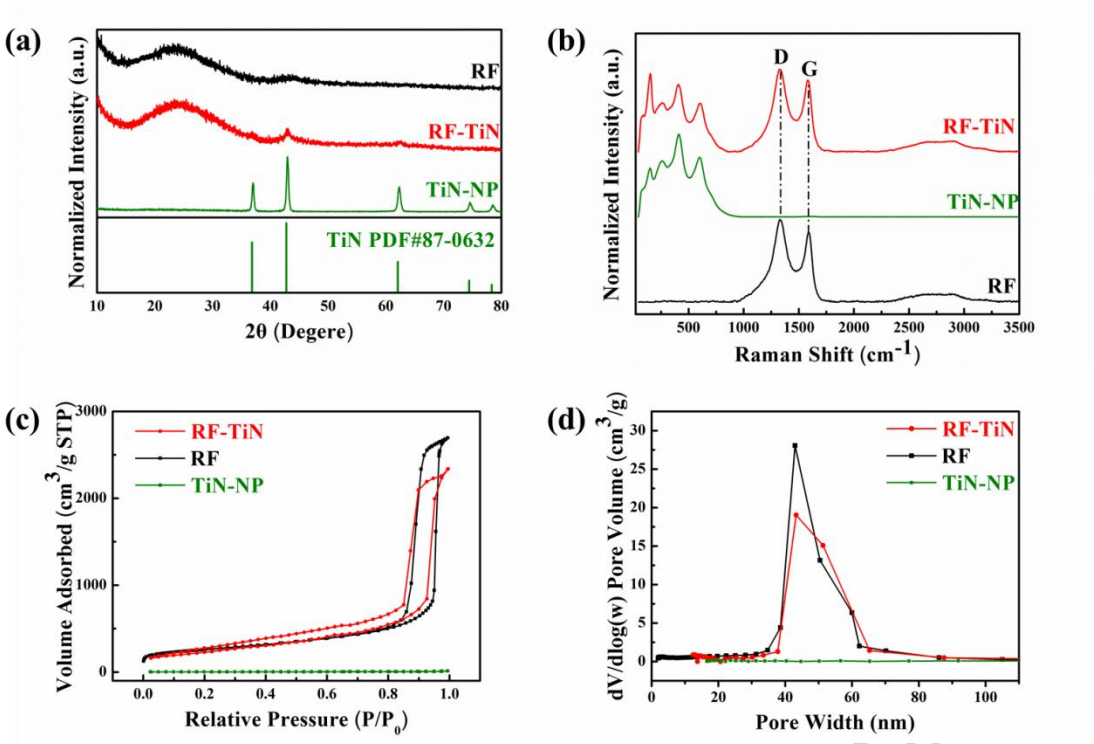

Figure 1 (a) XRD patterns of RF and RF-TiN. (b) Raman spectra of RF, RF-TiN and TiN-NP. (c) Nitrogen sorption isotherms of RF, RF-TiN and TiN-NP.. (d) Corresponding pore size distribution of RF, RF-TiN and TiN-NP.

To find out whether TiN nanoparticles were loaded on the surface or in the pores of the porous carbon, the porosity was investigated by the Brunauer–Emmett–Teller (BET) test. As measured by a N_2 adsorption/desorption, the surface area of RF is about 900 m^2/g with a pore volume of 4.12 cm^3/g. **Figure 1c** shows a type IV isotherm for mesoporous carbon with a characteristic hysteresis between adsorption/desorption curves in the medium relative pressure range. Correspondingly, the pore size distribution (PSD) result displays only one peak at 42 nm in **Figure 1d**, indicating a very narrow pore size distribution. After TiN incorporation, the surface area drops to 831 m^2/g while the pore volume shrinks to 3.14 cm^3/g. These changes were also reflected in the isotherm curve and PSD plot, which maintained similar shapes except with decreased absorbed pore volumes. The above BET results confirm that TiN nanoparticles were precisely loaded into the pores. This small crystallite size benefits from

the water vapor confined in the pores of porous carbon; the limited amount of which further determines the crystallite size of TiO_2 as the product of hydrolysis reaction. In the subsequent nitridation reaction, TiO_2 was converted directly into TiN without particle agglomeration and crystallite growth due to the pore confinement effect. Different from RF-TiN, the poor porosity and low surface area of TiN-NP was due to the particle agglomeration without carbon pore confinement in the RF-TiN case.

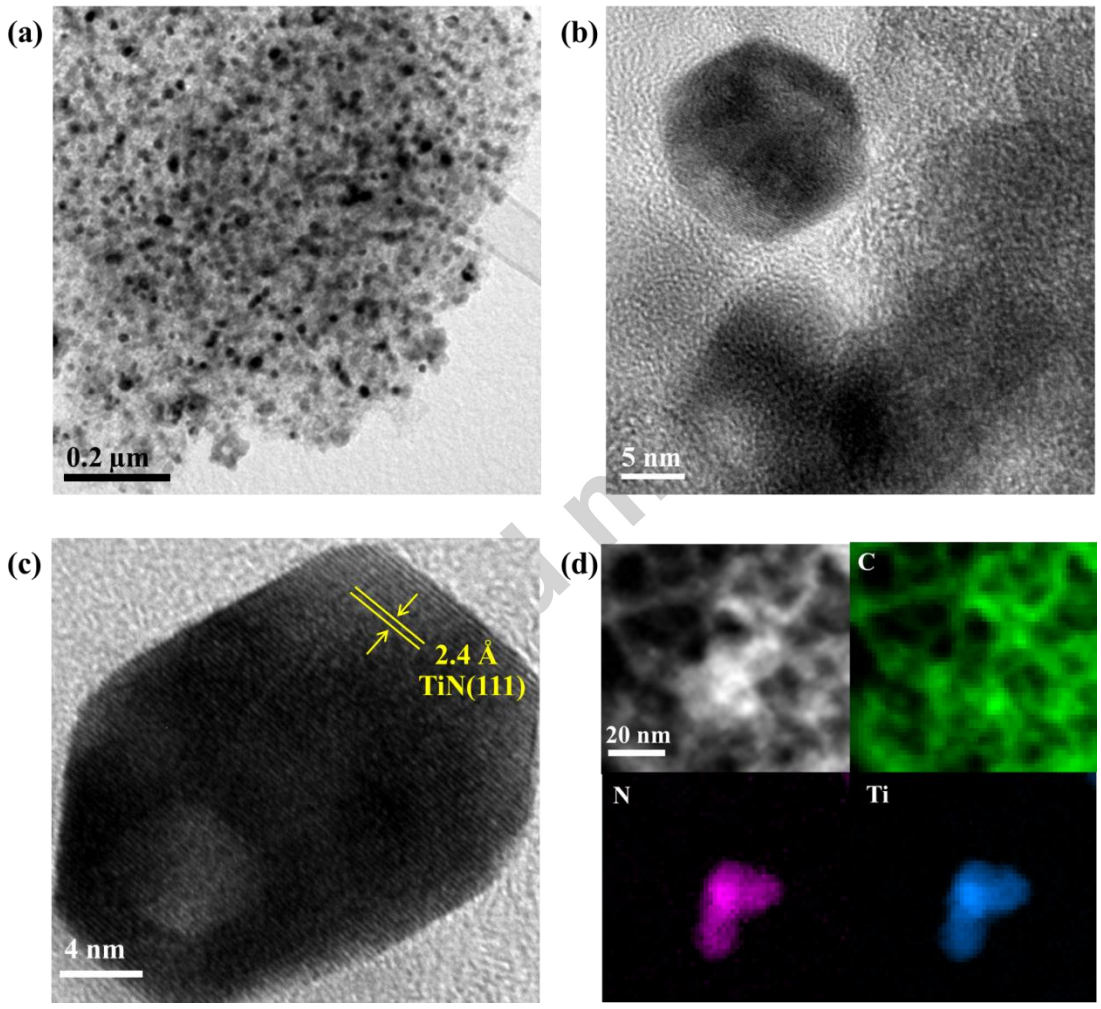

Figure 2 (a) TEM images of RF-TiN. (b), (c) TEM images of RF-TiN at high resolution. (d) Carbon, nitrogen and titanium EELS mappings of RF-TiN.

As shown in the transmission electron microscopy (TEM) images of **Figure 2a**, the dark particles of TiN, proved by electron energy loss spectroscopy (EELS) mapping in **Figure 2d**,

were distributed throughout the porous carbon host. At a higher resolution, the pore-loaded TiN structure is clearly seen in **Figure 2b**, with a d-spacing of 2.4 Å along (111) direction in **Figure 2c**. Compared with EELS mapping result, the signals of Ti are scarcely detected in the x-ray photoelectron spectroscopy (XPS) in **Figure 3a**. However, these seemingly contradictory results between EELS and XPS actually confirm the pore-loaded TiN structure since XPS is only a surface characterization method, further confirming TiN nanoparticles loaded inside the pores rather than on the carbon surface. The above TEM images and contrasting XPS/EELS results correspond well with the PSD results.

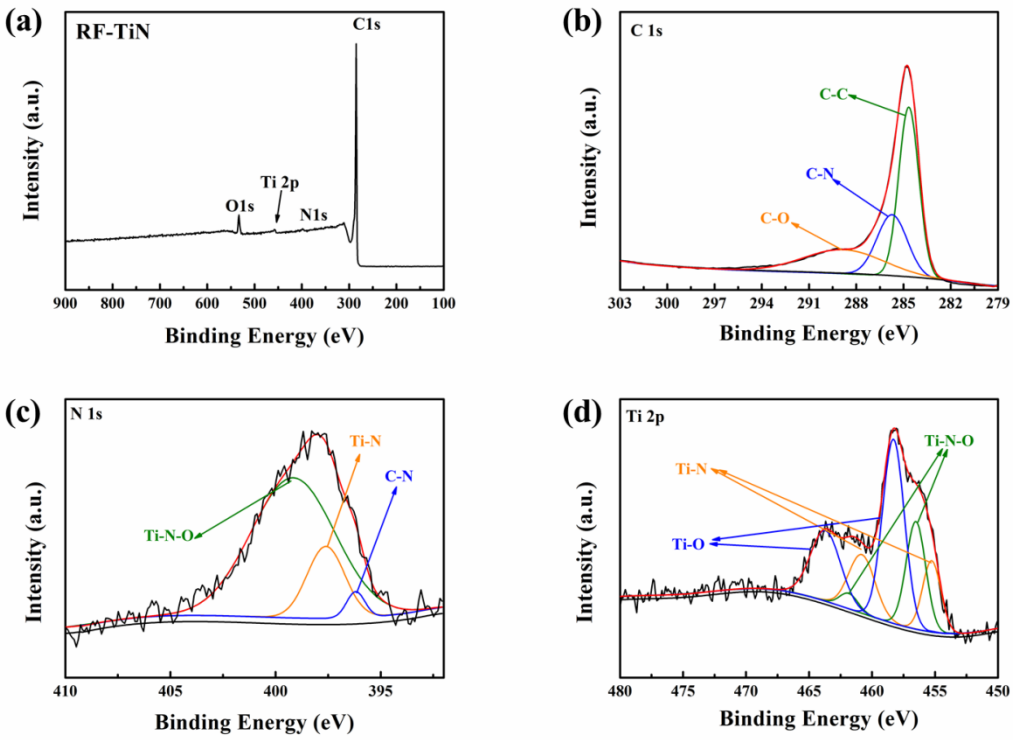

Figure 3 (a) XPS survey of RF-TiN. (b) XPS C1s spectra of RF-TiN. (c) XPS N1s spectra of RF-TiN. (d) XPS Ti 2p spectra of RF-TiN.

Till now, the pore-loaded TiN structure was fully demonstrated by the XRD, Raman, BET, and TEM characterizations. However, the detailed chemical bonding information of this novel structure is still inadequate although the XPS survey and EELS provided some preliminary results of element distribution. Under the high resolution XPS in **Figure 3b**, the

carbon 1s peak was deconvoluted into three peaks located at 284.6 eV, 285.7 eV, and 288.8 eV for C-C, C-N and C-O bonding, respectively. Especially, the existence of C-N bonding indicated the doping of N atoms into the carbon lattice fringe [42]. With respect to the N 1s and Ti 2p high resolution spectra, the existence of Ti-N bonding was confirmed in **Figure 3c** and **Figure 3d**. Here, it should be noted that inevitable surface oxidation of TiN during handling leads to the formation of Ti-N-O and Ti-O bonding [43].

Thus far, these complementary results highlight the loading of TiN nanoparticles into the recesses of the pores of N-doped carbon. This particular structural design possesses the following advantages in the electrochemical characterizations. Firstly, the high electronic conductivity from the TiN nanoparticles and NH_3-trimmed carbon host, greatly facilitate electron transfer. Secondly, loading TiN nanoparticles into the pore's recesses rather than onto the surface will fully expose the adsorptive sites and prevent TiN aggregation near the pore opening, which would otherwise lead to blocking future sulfur infiltration and Li^+ diffusion. Most importantly, the physical adsorption from the pore structure and chemical adsorption from nanosized TiN and N-doping enables a strong binding with polysulfide.

The above advantages suggests RF-TiN as a desirable cathode host for Li-S batteries. To prove this, RF-TiN was impregnated with sulfur, at a 70% mass content from TGA measurement in **Figure S5**, after heating the RF-TiN/ sulfur mixture under air at 155 °C for 12h under Ar. Revealed by scanning electron microscope (SEM), energy dispersive spectroscopy (EDS) and XRD patterns analysis in **Figure S6** and **Figure S7**, sulfur was uniformly distributed on the RF-TiN host. Then, the electrodes were prepared by the doctor-blade method and assembled with Li-metal in coin cells. As a control, RF and TiN-NP as cathode hosts were also tested in a Li-S battery prepared by the same process. All three hosts impregnated with sulfur are denoted as S@RF-TiN, S@RF, and S@TiN-NP, respectively.

In **Figure 4a** at a current density of 0.1C (1C=1672 mAh/g), S@RF-TiN shows a typical potential profile for Li-S batteries in the galvanostatic charge–discharge test. In the first discharge cycle, the plateau located at 2.3 V (vs. Li^+/Li, hereinafter inclusive) corresponds to the conversion from sulfur to Li_2S_x ($4 \leq x \leq 8$). With further discharge, another plateau appears at 2.14 V, corresponding to the formation of Li_2S_x ($2 \leq x \leq 4$) and lastly, Li_2S. In the subsequent charge process, the two plateaus seemingly merged into one slope, each of which corresponds to the short-chain polysulfide and long-chain polysulfide formation, respectively. With a discharge capacity of 1338 mAh/g and a charge capacity of 1265 mAh/g, the Coulombic efficiency is approximately 94.46 %, which is due to the partial dissolution of polysulfide into the electrolyte. This high charge capacity benefits from catalytic role of the TiN nanoparticles inside the carbon pores in accelerating the electrochemical reaction kinetics at the second plateau, a redox mediator effect on transferring of S_8 to polysulfides and back to Li_2S, which have been demonstrated before [34]. Compared with S@RF-TiN, S@RF and S@TiN-NP exhibit similar charge/discharge curves in the first cycle. However, the potential hysteresis of S@RF and S@TiN-NP is larger than that of S@RF-TiN, which is attributed to the slower reaction kinetics and associated electron transfer/Li^+ diffusion. Specifically, the low electronic conductivity of RF could not match the faster Li^+ diffusion capability and leads to an increased overpotential, though RF, with a larger surface area and pore volumes than RF-TiN, may possess a little higher Li^+ diffusion capabilities. As for TiN-NP, there is hardly any Li^+ diffusion pathway, proved by its poor porosity in **Figure 1d**, in the nonporous structure albeit TiN-NP possessing a much higher conductivity than RF-TiN. Therefore, the extremely poor Li^+ diffusion circumstance of TiN-NP results in a significantly larger potential hysteresis, in agreement with the lack of kink at the end of discharge, which corresponding to irreversible decomposition of $LiNO_3$ in the RF-TiN and RF cases [44, 45]. With respect to capacity, S@RF delivers a discharge capacity of 1102 mAh/g, while S@TiN-NP possesses a discharge

capacity of 800 mAh/g. As we know, an increased overpotential leads to an incomplete electrochemical reaction, and subsequently, a lowered capacity, which appears to be the case for S@RF and S@TiN-NP.

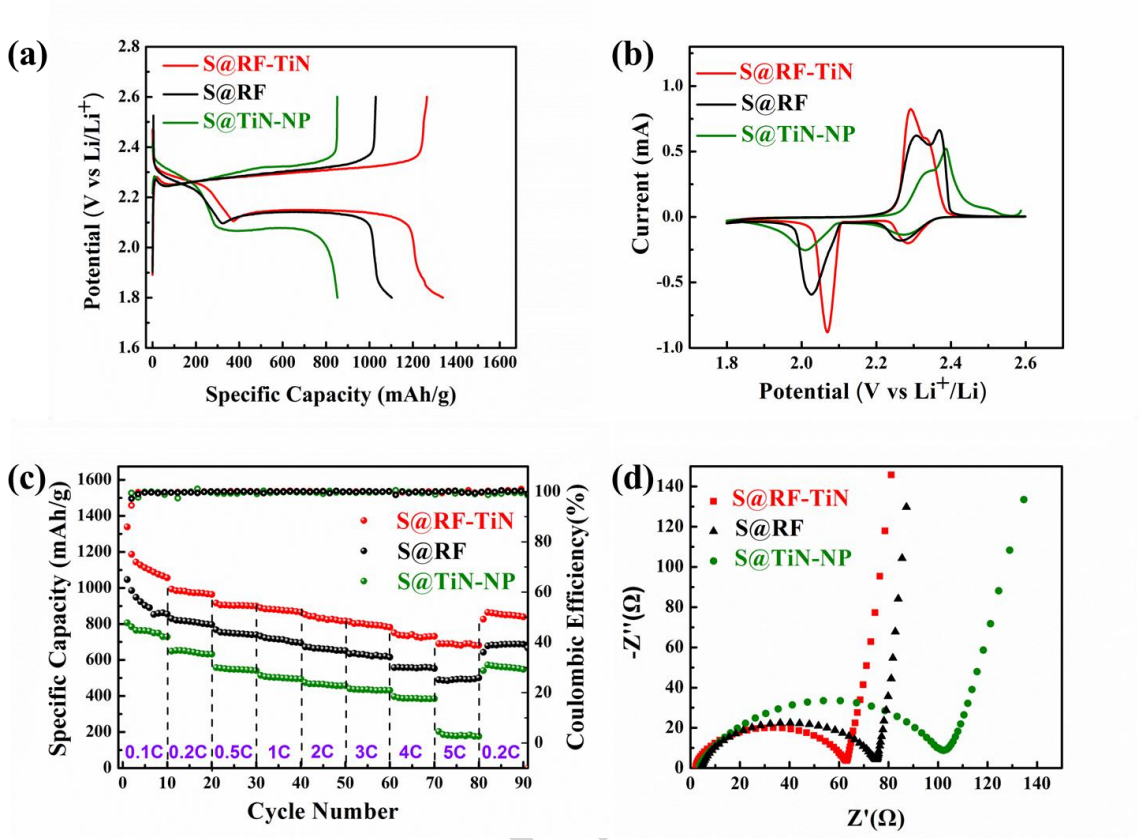

Figure 4 (a) Galvanostatic charge/discharge potential profiles of S@RF, S@RF-TiN and S@TiN-NP in the potential range of 1.8–2.6 V vs. Li^+/ Li at a current density of 0.1C. (b) CV curves of S@RF, S@RF-TiN and S@TiN-NP at a scanning rate of 0.05 mV/s. (c) Rate performance for S@RF, S@RF-TiN and S@TiN-NP at current density from 0.1C, 0.2C, 0.5C, 1C, 2C, 3C and 4C to 5C. (d) Nyquist plots of S@RF, S@RF-TiN and S@TiN-NP. All the electrochemical tests in the Figure 4 are obtained by using 1.5 mg/cm^2 active mass loading with a electrolyte/sulfur ratio of 16 ml/g_{sulfur}.

The electrochemical discrepancy in the galvanostatic charge–discharge test among S@RF-TiN, S@RF and S@TiN-NP is further expounded in the cyclic voltammetry (CV) test in **Figure 4b**. Compared with S@RF-TiN, the redox peak of S@RF and S@TiN-NP shift

downwards during the anodic scan and upwards during the cathodic scan, which is a result of the deficient electron transfer or Li^+ diffusion discussed previously. Moreover, the area changes amongst S@RF-TiN, S@RF and S@TiN-NP under redox peaks in **Figure 4b** are in line with the capacity variation in **Figure 4a**.

As discussed above, the advantage of RF-TiN with its fast and balanced electron transfer/Li^+ diffusion has been revealed under the galvanostatic test at a 0.1C current density. This merit was derived from the precise structural design, which was further confirmed under the rate test shown in **Figure 4c**. Notably, the high capacity was retained at 690 mAh/g under a 5C current density for S@RF-TiN. However, these values only reach 490 and 180 mAh/g for S@RF and S@TiN-NP, respectively. Based on the ratio between capacities under 0.1C and 5C, the capacity retention is about 53% for S@RF-TiN while only 44.4% for S@RF and 22.5% for S@TiN-NP.

This fast and balanced electron transfer/Li^+ diffusion of RF-TiN is not only demonstrated in the rate test, but also confirmed in the electrochemical impedance spectroscopy (EIS). From **Figure 4d**, we find that the Nyquist plots in the complex plane are comprised of a semicircle and a line, corresponding to the charge transfer resistance and Li^+ diffusion in the bulk electrolyte, respectively. In particular, the charge transfer resistance of S@RF-TiN is only about 31Ω, which is much smaller than 38Ω for S@RF and 51Ω for S@TiN-NP. It should be noted that the charge transfer resistance is determined by the electronic conductivity and Li^+ diffusion capability. Therefore, we can conclude that S@RF-TiN contributes to a faster electron transfer and Li^+ diffusion than S@RF and S@TiN-NP. In summation, the results of: the decreased potential hysteresis and increased capacity from the galvanostatic test, the decreased overpotential from the CV test, and decreased charge transfer resistance from the EIS test, suggest that RF-TiN enables a faster and more balanced electron transfer/Li^+

diffusion, and thus better electrochemical kinetics than RF and TiN-NP.

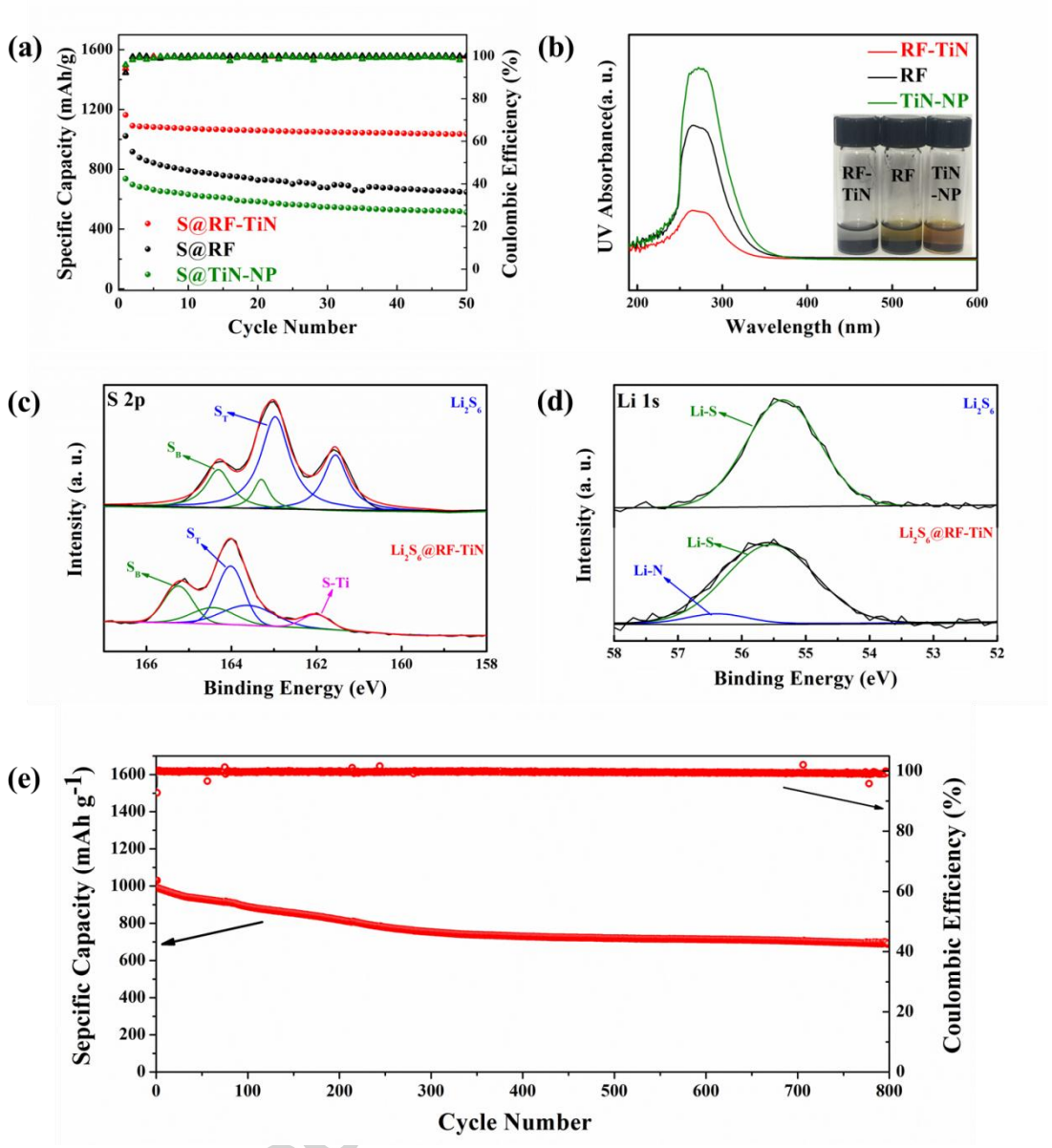

Figure 5 (a) Long-term cycling performance of S@RF, S@RF-TiN and S@TiN-NP at a current density of 0.2 C. (b) UV-vis absorption spectra of the Li_2S_x in DOL/DME solution after absorption by RF, RF-TiN and TiN-NP, respectively. Inset: Corresponding optical images. (c) XPS S 2p spectra of polysulfide before and after adsorption by RF-TiN. (d) XPS Li 1s spectra of polysulfide before and after adsorption by RF-TiN. (e) Long-term cycling performance of S@RF-TiN at a current density of 1C. All the electrochemical tests in the Figure 5 are obtained by using 1.5 mg/cm^2 active mass loading with a electrolyte/sulfur ratio of 16 ml/g_{sulfur}.

Thus far, we have demonstrated that the rational design of RF-TiN is conducive to a higher capacity and better rate capability. As described previously, this combination of a porous structure, N-doping and TiN loading also leads to a strong polysulfide adsorption. It can be seen from the data in **Figure 5a** that the capacity of S@RF-TiN drops from 1163 mAh/g to 1036 mAh/g with retention of 89.1 % after 50 cycles under a current density of 0.2 C. In contrast with S@RF-TiN, the capacity of S@RF can only be maintained at 63.3 %, dropping from 1022 mAh/g to 648 mAh/g after 50 cycles under the same testing conditions. Based on the prior comparison, it is clear that the polysulfide dissolution decreased after the additional synergic chemical adsorption from the N-doping and TiN nanoparticles found within the pores. As for S@TiN-NP, the capacity retention was only 69.4 % based on an initial capacity of 736 mAh/g and capacity of the fiftieth cycle. This result should be ascribed to the insufficient physical adsorption of TiN-NP due to its low surface area as shown in **Figure 1c** and resulting active sites restriction, despite the strong binding energy between TiN and polysulfide, which has already been affirmed by theoretical calculations [34]. The polysulfide reservoir of RF-TiN is superior to RF and TiN-NP, which is further demonstrated in **Figure 5b inset**. After immersing RF-TiN, RF, and TiN-NP in Li_2S_x in 1,2-dimethoxyethane (DME) and 1,3-dioxolane (DOL) (1:1 by volume) for 12 hours, the polysulfide adsorption capability among these three samples were visually distinguishable. The color of the Li_2S_x solution in the RF-TiN vial became colorless, while Li_2S_x in the RF and TiN-NP vials remained yellowish. The quantitative comparison is further revealed by ultraviolet (UV) spectroscopy. As shown in **Figure 5b**, the intensity of the peaks at 270 nm coincide with the amount of lingering S_4^{2-}/S_6^{2-} species after 12 hours of adsorption. In addition to the color change, RF-TiN showed the strongest polysulfide adsorption ability, attributing to the combined physical adsorption from porous structure and chemical adsorption from N-doping/TiN anchor. From another aspect, the strong polysulfide adsorption of RF-TiN is also revealed by XPS results.

Compared with Li_2S_6 in **Figure 5c**, both terminal (S_T) and bridging sulfur (S_B), after adsorption by RF-TiN, shifted to a higher binding energy location indicating a reduction in the electron cloud density from the attraction of N-doping or TiN nanoparticles [46, 47]. A more substantial evidence for polysulfide adsorption was supported by the appearance of Ti-S bonding at 162 eV [48]. Moreover, the Li 1s XPS spectra in Figure 5d experienced similar upshifts to the S 2p spectra due to the existence of Li-N bonding [49, 50]. Finally, the strong polysulfide immobilization of S@RF-TiN was confirmed at a 0.04% capacity fading per cycle under a 1C current density in **Figure 5e**. The capacity merely dropped from 1030 mAh/g to 700 mAh/g after 800 cycles.

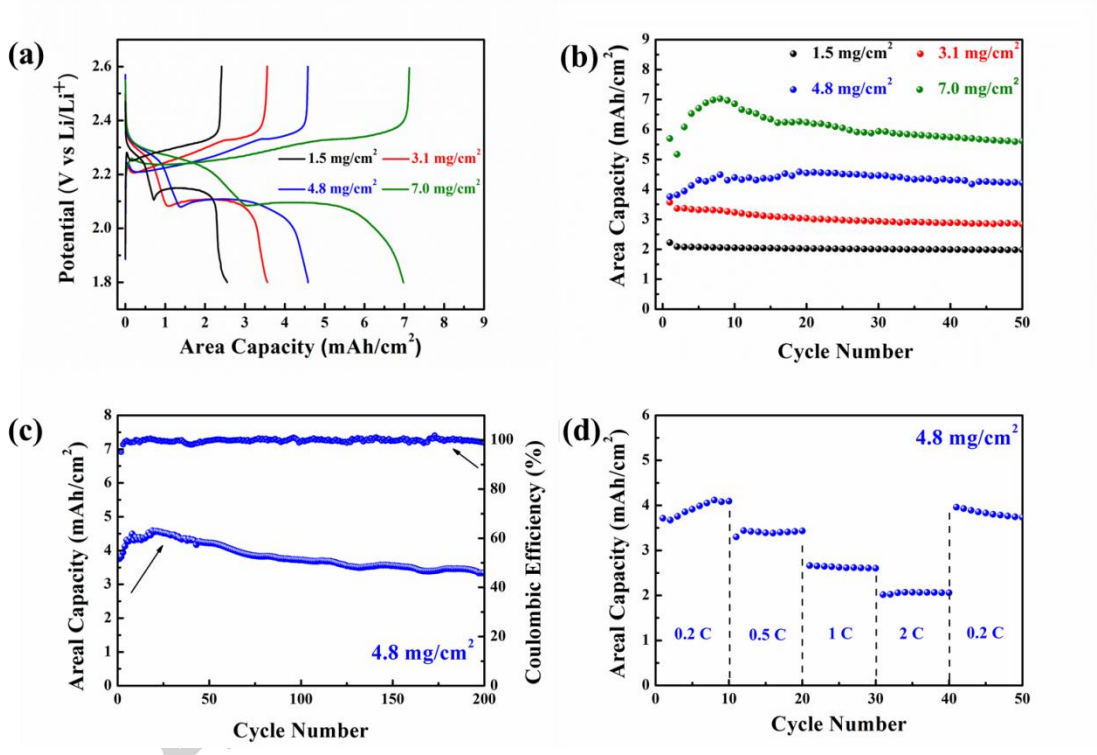

Figure 6 (a) Galvanostatic charge/discharge profiles of S@RF-TiN and (b) cycling performance of S@RF-TiN at various mass loadings at a current density of 0.2 C. (c) Long cycling performance of S@TiN-NP at a mass loading of 4.8 mg/cm^2 under current density of 0.2C. (d) Rate performance of S@TiN-NP at a mass loading of 4.8 mg/cm^2 under current density from 0.2C, 0.5C, 1C, to 2C. The ratio for electrolyte/sulfur in each cell is about 16 ml/g_{sulfur} for the mass loading of 1.5 mg/cm^2 while 10 ml/g_{sulfur} for the mass loading of 3.1

mg/cm^2, 4.8 mg/cm^2 and 7.0 mg/cm^2.

As mentioned beforehand, Li-S batteries may potentially become the primary power source for electric vehicles and portable electronics in replacing LIBs, therefore a high mass-loaded prototyping is required. To prove the feasibility of RF-TiN, we prepared electrodes with different sulfur loadings: at 1.5 mg/cm^2, 3.1 mg/cm^2, 4.8 mg/cm^2 to 7 mg/cm^2. With the increased sulfur loadings in **Figure 6a**, the corresponding area capacity also increased from 2.5 mAh/cm^2 to 3.5 mAh/cm^2, 4.5 mAh/cm^2, and 7 mAh/cm^2, well above the levels of commercial LIBs. Compared with common mass loading of 1.5 mg/cm^2, the high mass loading of 7 mg/cm^2 did not lead to a substantial drop in capacity nor elevated overpotential, which should be attributed to the pivotally high electronic conductivity and facile Li^+ diffusion ability. Moreover, the cycling performance at a high mass loading was also demonstrated in **Figure 6b**. With the proficient polysulfide anchoring in preventing large amounts of polysulfide dissolution, the cycling of the high mass loaded cell showed impressive areal capacity retention. As a result, the areal capacity of 7 mg/cm^2 mass loading could still remain 5.9 mAh/cm^2 after 50 cycles. Moreover, the area capacity retention can be high up to 88.8% after 200 cycles, under a relatively low mass loading of 4.8 mg/cm^2 as shown **Figure 6c**. Finally, the rate capability under high mass loading of 4.8 mg/cm^2 was examined in **Figure 6d**. At various current densities from 0.2C, 0.5C, 1C, to 2C, the corresponding area capacity was around 4 mAh/cm^2, 3.5 mAh/cm^2, 2.6 mAh/cm^2 and 4 mAh/cm^2, 2.1 mAh/cm^2 respectively. The excellent rate performance under high mass loading and high current density fully demonstrated the advanced kinetic behaviors of RF-TiN, which is due to its high electronic conductivity and fast Li^+ diffusion ability.

Conclusion

In conclusion, this is the first report of TiN embedded within the pores of N-doped carbon,

which acted as a cathode host for Li-S batteries, and exhibited excellent electrochemical performance. After nitridation of water vapor loaded TiO_2, the TiN nanoparticles confined within the pores of N-doped carbon offered the following advantages: a high electronic conductivity inherited from the TiN/carbon host, strong polysulfide anchoring realized by the physical adsorption of the porous carbon structure, and chemical adsorption from N-doping/TiN. Moreover, TiN nanoparticles were loaded into the pore recesses, rather than onto the surface, which prevents the blockage of subsequent sulfur infiltration and Li^+ ion diffusion. In the consequent electrochemical tests, the high capacity of 1338 mAh/g (at a current density of 0.1 C), decent rate capability, and high mass loading (up to 7 mg/cm^2), all benefitted from the fast electron transfer and facile Li^+ ion diffusion. In addition, the stable cycling with a decay of 0.04% per cycle over 800 cycles can be attributed to the combined physical and chemical polysulfide adsorption. Finally, this special structure of TiN nanoparticles embedded in carbon pores can potentially possess wider applications in metal air batteries, fuel cells and other energy storage areas.

Acknowledgements

The authors express their appreciation to the University of Waterloo, Natural Sciences and Engineering Research Council of Canada (NSERC) and the Waterloo Institute for Nanotechnology for their financial support. The authorship also gratefully acknowledges the Canadian Center for Electron Microscopy (CCEM) at McMaster University for TEM and EELS characterization.

Appendix A. Supplementary material

Supplementary data associated with this article can be found in the online version at http://dx.doi.org/10.1016

Reference

[1] Z.P. Cano, D. Banham, S. Ye, A. Hintennach, J. Lu, M. Fowler, Z. Chen, Nature Energy, 3 (2018) 279.
[2] Z. Xing, S. Wang, A. Yu, Z. Chen, Nano Energy, (2018).
[3] J.A. Lochala, H. Zhang, Y. Wang, O. Okolo, X. Li, J. Xiao, Small Methods, (2017).
[4] L. Lu, X. Han, J. Li, J. Hua, M. Ouyang, J Power Sources, 226 (2013) 272.
[5] N.S. Choi, Z. Chen, S.A. Freunberger, X. Ji, Y.K. Sun, K. Amine, G. Yushin, L.F. Nazar, J. Cho, P.G. Bruce, Angewandte Chemie International Edition, 51 (2012) 9994.
[6] C. Zhan, Z. Yao, J. Lu, L. Ma, V.A. Maroni, L. Li, E. Lee, E.E. Alp, T. Wu, J. Wen, Nature Energy, 2 (2017) 963.
[7] M. Ko, S. Chae, J. Ma, N. Kim, H.-W. Lee, Y. Cui, J. Cho, Nature Energy, 1 (2016) 16113.
[8] P.G. Bruce, S.A. Freunberger, L.J. Hardwick, J.-M. Tarascon, Nat Mater, 11 (2012) 19.
[9] G. Li, Z. Chen, J. Lu, Chem, 4 (2018) 3.
[10] J. Lochala, D. Liu, B. Wu, C. Robinson, J. Xiao, ACS applied materials & interfaces, 9 (2017) 24407.
[11] J. Xiao, Adv Energy Mater, 5 (2015) 1501102.
[12] G. Li, S. Wang, Y. Zhang, M. Li, Z. Chen, J. Lu, Adv Mater, (2018) 1705590.
[13] T. Cleaver, P. Kovacik, M. Marinescu, T. Zhang, G. Offer, J Electrochem Soc, 165 (2018) A6029.
[14] X. Ji, K.T. Lee, L.F. Nazar, Nat Mater, 8 (2009) 500.
[15] G. Tan, R. Xu, Z. Xing, Y. Yuan, J. Lu, J. Wen, C. Liu, L. Ma, C. Zhan, Q. Liu, Nature Energy, 2 (2017) 17090.
[16] X. Ji, S. Evers, R. Black, L.F. Nazar, Nat Commun, 2 (2011) 325.
[17] J. Song, M.L. Gordin, T. Xu, S. Chen, Z. Yu, H. Sohn, J. Lu, Y. Ren, Y. Duan, D. Wang, Angewandte Chemie International Edition, 54 (2015) 4325.
[18] L. Kong, B.Q. Li, H.J. Peng, R. Zhang, J. Xie, J.Q. Huang, Q. Zhang, Adv Energy Mater, (2018) 1800849.
[19] T.Z. Hou, X. Chen, H.J. Peng, J.Q. Huang, B.Q. Li, Q. Zhang, B. Li, Small, 12 (2016) 3283.
[20] X. Chen, H.-J. Peng, R. Zhang, T.-Z. Hou, J.-Q. Huang, B. Li, Q. Zhang, ACS Energy Letters, 2 (2017) 795.
[21] F. Liu, Q. Xiao, H.B. Wu, F. Sun, X. Liu, F. Li, Z. Le, L. Shen, G. Wang, M. Cai, Acs Nano, 11 (2017) 2697.
[22] J. Song, Z. Yu, M.L. Gordin, D. Wang, Nano Lett, 16 (2016) 864.
[23] J. Song, M.L. Gordin, T. Xu, S. Chen, Z. Yu, H. Sohn, J. Lu, Y. Ren, Y. Duan, D. Wang, Angewandte Chemie, 127 (2015) 4399.
[24] W. Zhou, C. Wang, Q. Zhang, H.D. Abruña, Y. He, J. Wang, S.X. Mao, X. Xiao, Adv Energy Mater, 5 (2015) 1401752.
[25] F. Hippauf, W. Nickel, G.P. Hao, K. Schwedtmann, L. Giebeler, S. Oswald, L. Borchardt, S. Doerfler, J.J. Weigand, S. Kaskel, Advanced Materials Interfaces, 3 (2016) 1600508.
[26] L. Kong, X. Chen, B.Q. Li, H.J. Peng, J.Q. Huang, J. Xie, Q. Zhang, Adv Mater, 30 (2018) 1705219.
[27] X. Liu, J.Q. Huang, Q. Zhang, L. Mai, Adv Mater, (2017).
[28] W. Zhou, X. Xiao, M. Cai, L. Yang, Nano Lett, 14 (2014) 5250.
[29] Z. Hao, L. Yuan, C. Chen, J. Xiang, Y. Li, Z. Huang, P. Hu, Y. Huang, Journal of

Materials Chemistry A, 4 (2016) 17711.
[30] N. Mosavati, V.R. Chitturi, S.O. Salley, K.S. Ng, J Power Sources, 321 (2016) 87.
[31] X. Wang, V. Raju, W. Luo, B. Wang, W.F. Stickle, X. Ji, Journal of Materials Chemistry A, 2 (2014) 2901.
[32] D.-R. Deng, T.-H. An, Y.-J. Li, Q.-H. Wu, M.-S. Zheng, Q.-F. Dong, Journal of Materials Chemistry A, 4 (2016) 16184.
[33] Z. Cui, C. Zu, W. Zhou, A. Manthiram, J.B. Goodenough, Adv Mater, 28 (2016) 6926.
[34] T.-G. Jeong, D.S. Choi, H. Song, J. Choi, S.-A. Park, S.H. Oh, H. Kim, Y. Jung, Y.-T. Kim, ACS Energy Letters, 2 (2017) 327.
[35] Y. Wang, R. Zhang, Y.-c. Pang, X. Chen, J. Lang, J. Xu, C. Xiao, H. Li, K. Xi, S. Ding, Energy Storage Materials, 16 (2019) 228.
[36] J. Brückner, S. Thieme, H.T. Grossmann, S. Dörfler, H. Althues, S. Kaskel, J Power Sources, 268 (2014) 82.
[37] Z. Xing, Y. Qi, Z. Tian, J. Xu, Y. Yuan, C. Bommier, J. Lu, W. Tong, D.-e. Jiang, X. Ji, Chem Mater, 29 (2017) 7288.
[38] W. Shen, Z. Li, Y. Liu, Recent Patents on Chemical Engineering, 1 (2008) 27.
[39] Z. Xing, N. Gao, Y. Qi, X. Ji, H. Liu, Carbon, 115 (2017) 271.
[40] Z. Xing, Y. Qi, Z. Jian, X. Ji, ACS applied materials & interfaces, 9 (2016) 4343.
[41] Z. Xing, X. Luo, Y. Qi, W.F. Stickle, K. Amine, J. Lu, X. Ji, ChemNanoMat, 2 (2016) 692.
[42] R. Karunagaran, T.T. Tung, C. Shearer, D. Tran, C. Coghlan, C. Doonan, D. Losic, Materials, 10 (2017) 921.
[43] Y. Han, X. Yue, Y. Jin, X. Huang, P.K. Shen, Journal of Materials Chemistry A, 4 (2016) 3673.
[44] A. Rosenman, R. Elazari, G. Salitra, E. Markevich, D. Aurbach, A. Garsuch, J Electrochem Soc, 162 (2015) A470.
[45] S.S. Zhang, J Power Sources, 322 (2016) 99.
[46] Y.-S. Su, Y. Fu, T. Cochell, A. Manthiram, Nat Commun, 4 (2013) 2985.
[47] G. Li, W. Lei, D. Luo, Y.P. Deng, D. Wang, Z. Chen, Adv Energy Mater, 8 (2018) 1702381.
[48] T. Lin, C. Yang, Z. Wang, H. Yin, X. Lü, F. Huang, J. Lin, X. Xie, M. Jiang, Energ Environ Sci, 7 (2014) 967.
[49] T.-Z. Hou, W.-T. Xu, X. Chen, H.-J. Peng, J.-Q. Huang, Q. Zhang, Angewandte Chemie International Edition, (2017).
[50] S. Ishiyama, Y. Baba, R. Fujii, M. Nakamura, Y. Imahori, Materials Transactions, 54 (2013) 2233.

Zhenyu Xing graduated with B.Sc. of chemistry from Jilin University in 2012. He earned his Ph.D. in chemistry from Oregon State University in 2016 under the supervision of Prof. Xiulei Ji. He did his Postdoc research with Prof. Zhongwei Chen at University of Waterloo since 2017. Currently, he is an Associate Professor in School of Chemistry and Environment

at South China Normal University. His research focuses on preparation, structure, property and application of porous carbon materials.

Gaoran Li is currently a postdoctoral researcher in the Department of Chemical Engineering, University of Waterloo, Canada. He received his Ph.D. degree in Chemical Engineering from the College of Chemical and Biological Engineering, Zhejiang University, in 2016. His research interests focus on energy-storage materials for advanced lithium-ion and lithium-sulfur batteries.

Serubbabel Sy graduated with a BASc. in Chemical Engineering from University of Waterloo in 2012. He worked for a year at Syngenta, before returning to completing his MASc also in Chemical Engineering from University of Waterloo in 2015 under the supervision of Prof. Aiping Yu. Currently, he is working on his Ph.D. with Prof. Aiping Yu and Prof Zhongwei Chen at the University of Waterloo. His research focus is on the preparation, structural design and properties of graphene materials for the use in energy related applications.

Dr. Zhongwei Chen is Canada Research Chair Professor in Advanced Materials for Clean Energy at University of Waterloo. His research interests are in the development of advanced energy materials for metal-air batteries, lithiumion batteries and fuel cells. He has published 1

book, 7 book chapters and more than 150 peer reviewed journal articles with over 10,000 citations with H-index 50 (Google Scholar). He is also listed as inventor on 15 US/international patents, with several licensed to companies in USA and Canada. He was recipient of the 2016 E. W. R Steacie Memorial Fellowship, which followed shortly upon several other prestigious honors, including the Ontario Early Researcher Award, an NSERC Discovery Supplement Award, the Distinguished Performance and the Research Excellence Awards from the University of Waterloo.

Highlights

1 First recessed deposition of TiN into N-doped carbon as Li-S battery cathode host

2. High conductivity and advanced chemical/physical polysulfide adsorption ability

3. Stable long cycling performance after 800 cycles and high mass loading up to 7 mg/cm^2